Available online at www.sciencedirect.com
SCIENCE DIRECT®
PERGAMON
International Journal of Heat and Mass Transfer 46 (2003) 4799–4811
International Journal of HEAT and MASS TRANSFER
www.elsevier.com/locate/ijhmt

Effect of magnetic field on *g*-jitter induced convection and solute striation during solidification in space

K. Li [a], B.Q. Li [a,*], H.C. de Groh [b]

[a] *School of Mechanical and Materials Engineering, Washington State University, Pullman, WA 99163, USA*
[b] *NASA Glenn Research Center, Cleveland, OH 44135, USA*

Received 10 November 2002; received in revised form 4 June 2003

Abstract

A 2-D finite element model is presented for the melt growth of single crystals in a microgravity environment with a superimposed DC magnetic field. The model is developed using deforming finite element methodology and predicts steady and transient convective flows, heat transfer, solute distribution, and solidification interface morphology associated with the melt growth of single crystals in microgravity with and without an applied magnetic field. Numerical simulations were carried out for a wide range of parameters including idealized microgravity condition, synthesized *g*-jitter and real *g*-jitter data taken by on-board accelerometers during space flights. The results reveal that the time varying *g*-jitter disturbances, although small in magnitude, cause an appreciable convective flow in the liquid pool, which in turn produces detrimental effects during the space processing of single crystal growth. An applied magnetic field of appropriate strength, superimposed on the microgravity, can be very effective in suppressing the deleterious effects resulting from *g*-jitter disturbances.

1. Introduction

Space flight experiments on the melt growth of single crystals indicate that natural convection induced by gravity perturbation or *g*-jitter has a strong influence on the defect formation in the crystals. One of the important characteristics of *g*-jitter induced convection is that it occurs mostly randomly in both direction and time, which is attributed to the nature of the *g*-jitter forces. During normal space flights, a gravity level of $10^{-6}g_0$ is established. This dynamic weightlessness condition experienced by flight vehicles is prone to perturbations that stem from a variety of sources, which include crew motions, mechanical vibrations (pumps, motors, excitations of natural frequencies of spacecraft structures), spacecraft maneuvers and attitude, atmospheric drag and the Earth's gravity gradient [1]. Detailed studies on *g*-jitter effects reveal that *g*-jitter induced convection in spacecraft is directly related to the magnitude and frequency of the gravity perturbation and to the alignment of the gravity field with respect to the growth direction or the direction of the temperature gradient [2–5]. Crystal growth experiments further indicate that residual gravity of $10^{-5}g_0$ is sufficient to cause appreciable fluid motion in the liquid, thereby resulting in the quality of the crystals being unacceptable. The orientation of the gravity vector with respect to the temperature gradient also plays an important role in convective melt flows. The velocity attains a maximum when the gravity vector is perpendicular to the temperature gradients [4,5].

Numerous numerical simulations have been conducted to understand and estimate the adverse effects of time varying *g*-jitter [4–10]. Both 2-D and 3-D numerical models have been developed for this purpose [4,5,11]. These models have been used to study the effects associated with both idealized single- and multiple-frequency *g*-jitter modulations and real *g*-jitter collected by accelerometers during actual flight experiments. These studies showed that the frequency, amplitude and spatial

* Corresponding author. Tel.: +1-509-335-7386; fax: +1-509-335-4662.
E-mail address: li@mme.wsu.edu (B.Q. Li).

0017-9310/$ - see front matter © 2003 Elsevier Ltd. All rights reserved.
doi:10.1016/S0017-9310(03)00336-3

Nomenclature

B_0	magnetic field magnitude scale
C	concentration
C_p	specific heat
C_0	concentration scale
D	solute diffusivity
Gr_T	thermal Grashof number
Gr_S	solutal Grashof number
g_0	earth gravity constant
H	latent heat of Bi
Ha	Hartmann number
$h(y)$	dimensionless x-position of growth interface
$\hat{i}, \hat{j}$	unit vector of ith, jth component
L	length of three zones
L_h	length of hot zone
L_c	length of cold zone
L_g	length of gradient zone
L_0	dimensionless x-position of hot end
L_1, L_4	dimensionless lower and upper y-positions of ampoule outer surface
L_2, L_3	dimensionless lower and upper y-position of ampoule inner surface
k	thermal conductivity
k_0	segregation coefficient
m	slope of solidus curve
$\hat{n}$	unit normal vector
p	pressure
Pr	Prandtl number
Sc	Schmidt number
Ste	Stefan number
S	absolute thermoelectric power
R_0	length scale
Ra	radiation number of ampoule
T	temperature
T^*	dimensional temperature
T_h	hot zone temperature
T_c	cold zone temperature
T_m	dimensionless melting point
T_{m0}	melting temperature of pure Bi
dT/dx	temperature gradient
ΔT	temperature scale
t_0	time scale
$\underline{U}_*$	velocity vector
U	interface velocity
U_0	velocity scale
u	x-direction velocity component
V_g	crystal pulling speed
V_p	dimensionless pulling speed
v	y-direction velocity component
W_i	inner width of ampoule
W_o	outer width of ampoule

Greek symbols

ρ_0	density of pure Bi at T_m
β_T	thermal expansion coefficient
β_C	solutal expansion coefficient
ν	kinematic viscosity
κ	thermal diffusivity
ε	penalty parameter for pressure
ε_{amp}	radiation coefficient of ampoule
Ω	computational domain
$\partial\Omega$	computational domain boundary
σ	Stefan–Bortzman constant
σ_m	electrical conductivity
δ_{ij}	delta function
ϕ	shape function for velocity
θ	shape function for temperature
ψ	shape function for pressure

Subscripts

cry	crystal
amp	ampoule
amb	ambient
i, j	ith, jth component

Superscript

T	matrix transpose

orientation of the residual gravity vector all play an important role in determining the convective flow behavior of the system. When the residual accelerations oscillate about the positive and negative of an axis, the orientation of this direction relative to the density gradient determines whether a mean flow is generated in the system [12]. Sinusoidal accelerations induce an oscillating convective flow and composition oscillation in the liquid. The resulting velocity and composition fields oscillate with the same frequency of the affecting gravity field. Benjapiyaporn et al. [13] reported a study on the g-jitter influence of solute transport and convection together with solidification in a planned space flight experiment configuration. They used the finite difference approximation for field calculations and the enthalpy method to model the solidification interface. In their calculations, the melting temperature of the pure solvent was used to determine the solidification interface. While the enthalpy method is very useful for alloy solidification with a distinctive mushy zone, it has inherent limitations in precisely capturing the solidification front of pure or nearly pure materials. They used simulated g-jitter data for their simulations to show that flow and segregation increase with decreasing g-jitter frequency and increasing amplitude. Their study further illustrates that the concentration can vary along the solidification

interface, suggesting that it is necessary to take into consideration the effects of concentration on the melting temperature to get an accurate estimate of interface shape.

The use of the magnetic field to control the melt motion during single crystal growth has been widespread in the semiconductor industry. Because the magnetic damping effect comes from a different origin from that of gravity reduction, it is plausible to suppress the *g*-jitter effects by imposing an appropriate magnetic field [14]. Studies on the *g*-jitter induced melt flows in the systems of relevance to space crystal growth experiments have been reported by Ma and Walker [12] and Baumgartl and Muller [11,15]. The former presented a semi-analytical model for the magnetic field effects on *g*-jitter driven thermal convection, while the latter presented a 3-D model of melt flow driven by a single frequency *g*-jitter force parallel to the thermal gradient with either transverse or axial fields imposed. Recently, Li and co-workers [7,14,16–21] have reported a series of studies, including both analytical analyses and numerical simulations, on the magnetic field effects on the *g*-jitter induced flows and mass transfer. Unlike others, their studies used both simulated *g*-jitter signatures and real *g*-jitter data taken from typical space flights, with the latter intended to obtain an understanding of the thermal and flow phenomena in a realistic *g*-jitter environment. In space vehicles, *g*-jitter is not aligned perfectly with the thermal gradient during crystal growth. The most deleterious flow effects, however, result from the *g*-jitter component that is perpendicular to the thermal gradient [4,5]. The melt flow in microgravity is shown to have a very strong effect on the solute transport. Their studies further demonstrate that these deleterious *g*-jitter effects can be suppressed by the application of an external magnetic field. Thus far, these studies have been primarily conducted on simplified configurations of the melt growth experiment furnace used for space flights in the presence of magnetic fields. None of these studies have considered the solidification behavior, which is a critical part of the process. Nonetheless, these studies have provided a useful basis upon which models incorporating more realistic issues such as solidification and ampoule configuration, coupled with more realistic thermal boundary conditions. These more realistic models will provide a much more powerful tool not only for enhancing our fundamental understanding of fluid mechanics and thermal phenomena in space crystal growth systems but also for developing rational guidelines for both space experiment design and interpretation of experimental measurements.

In the present study, a finite element model is presented for the heat and mass transfer and solidification phenomena associated with the melt growth of single crystals in microgravity with and without an imposed magnetic field. The analysis is based on a 2-D geometry. It is noted that for a solidification furnace of cylindrical geometry and terrestrial conditions, a 2-D axisymmetric condition can be established and maintained for field variables of interest [21]. In a microgravity environment, however, such an axisymmetric condition can not usually be maintained because frequent maneuvering of space vehicles changes the gravity orientation. It is also realized that because of the frequent change in gravity directions, the flow structure is truly three-dimensional and 3-D models should be developed to fully appreciate the complex 3-D flow structure [21]. Nonetheless, a 2-D analysis will provide some essential features of *g*-jitter induced flows and solidification behavior and thus form the required basis upon which 3-D models can be further developed. The 2-D analysis presented below is based on the solution of the Navier–Stokes equations for fluid flow, the energy balance equation for the temperature distribution and the mass balance equation for species transport in Sn-doped Bi alloy melt. The numerical scheme uses a quasi-Lagrangian deforming finite element approach where the solidification interface is tracked precisely by deforming the elements associated with the moving interface. This interface track approach allows us to accurately predict the interface shape change as a function of solute distribution, which is critical for space experiments but has not yet fully appreciated. Numerical simulations are conducted of the transient convective flows and solute redistribution in the melts and their effects on the solidification interface morphology under the combined action of *g*-jitter and external magnetic fields. Both synthetic *g*-jitter, which represents a single component of Fourier synthesis of *g*-jitter data, and real *g*-jitter data are used in the analyses.

2. Problem statement

Fig. 1 schematically illustrates the 2-D model used to study Bridgman–Stockbarger Sn-doped Bi single crystal growth in microgravity. An external DC magnetic field is applied along the thermal gradient. The ambient temperature profile (T_{amb}) consists a cold zone (T_c), a linear gradient zone (dT/dx) and a hot zone (T_h). In the present study, the pseudo-steady-state model [22] is adopted in which the translation of the ampoule is simulated by feeding the melt with the uniform impurity concentration C_0 into the inlet at the constant growth velocity V_g, while the crystal is withdrawn from the outlet at the speed that conserves the mass of the system. The length of the computation domain is L, the inner width of the ampoule is W_i and the outer width is W_o. The configuration described above is similar to that used for the MEPHISTO Space Flight experiments [6].

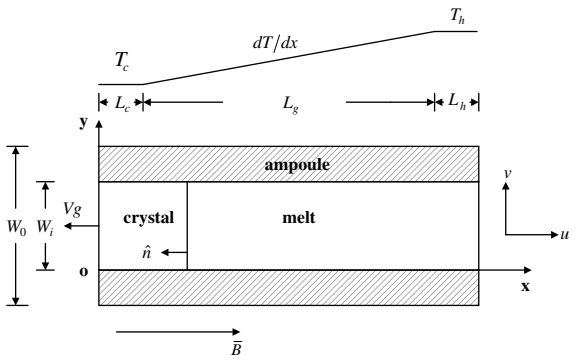

Fig. 1. Schematic representation of 2-D model for Bridgman Sn-doped Bi single crystal growth system in microgravity.

The residual acceleration experienced by the spacecraft in microgravity is composed of a steady acceleration component and a time-dependent acceleration component (g-jitter). The amplitude of the time-dependent component is much greater than that of the steady component. The real g-jitter data taken during space flight show that g-jitter changes both spatially and temporally. In some cases, to help analyses, g-jitter can be represented by the combination of a series of single frequency accelerations as follow:

$$\vec{g}(t) = \sum_{n=1}^{N} \vec{g}_n \sin(2\pi\omega_n t) \tag{1}$$

where $\vec{g}_n$ is the amplitude and ω_n the frequency associated with the nth component of g-jitter. Both the synthetic and real g-jitter data are considered in the present study.

The time-dependent phenomena of fluid flow, heat and mass transfer in the above system with the presence of an external magnetic field are described by the Navier–Stokes equations with the time varying gravity force and the Lorentz force resulting from the imposition of a magnetic field. For the melt flow, the standard Boussinesq approximation, $\rho = \rho_0[1 - \beta_T(T - T_{m0}) - \beta_C(C - C_0)]$, has been used. Furthermore, the thermoelectric effect, i.e., $\vec{J} = -S\nabla T$, is neglected, because of the lack of reliable data for the absolute thermoelectric power S of the fluid and also because it generates a flow component in the z-direction and thus violates the 2-D assumption. With an appropriate choice of scales, the governing equations may be non-dimensionalized and are given below. For the melt, these equations become

$$\nabla \cdot \vec{U} = 0 \tag{2}$$

$$\frac{\partial \vec{U}}{\partial t} + \vec{U} \cdot \nabla \vec{U} = -\nabla p + \nabla^2 \vec{U} - [Gr_T(T - T_m) + Gr_S(C - 1)]\vec{g}(t) + Ha^2(\vec{U} \times \vec{B} \times \vec{B}) \tag{3}$$

$$\frac{\partial T}{\partial t} + \vec{U} \cdot \nabla T = \frac{1}{Pr}\nabla^2 T \tag{4}$$

$$\frac{\partial C}{\partial t} + \vec{U} \cdot \nabla C = \frac{1}{Sc}\nabla^2 C \tag{5}$$

For the crystal and the ampoule, where a bulk flow is superimposed because of the choice of the coordinate system, only heat transfer analysis is needed. The solute diffusion in crystal is also ignored. With these simplifications, the governing equations can be written as follows:

$$\frac{\partial T_{cry}}{\partial t} + Vp(\hat{e}_x \cdot \nabla T_{cry}) = \frac{\kappa_{cry}}{\kappa}\frac{1}{Pr}\nabla^2 T_{cry} \tag{6}$$

$$\frac{\partial T_{amp}}{\partial t} + Vp(\hat{e}_x \cdot \nabla T_{amp}) = \frac{\kappa_{amp}}{\kappa}\frac{1}{Pr}\nabla^2 T_{amp} \tag{7}$$

In deriving the above equations, the following scales are used: $R_0 = 0.5W_i$ for length, $U_0 = v/R_0$ for velocity, $t_0 = R_0^2/v$ for time, $p_0 = \rho_0 U_0^2$ for pressure, C_0 for concentration, g_0 for gravity, B_0 for magnetic field, $\Delta T = (T_h - T_c)$ for temperature. The non-dimensional parameters are defined as

$$Gr_T = \beta_T R_0^3 g_0 \Delta T/v^2, \quad Gr_S = \beta_S R_0^3 g_0 C_0/v^2$$
$$T = (T^* - T_c)/\Delta T$$
$$Pr = v/\kappa, \quad Sc = v/D, \quad Ra = \varepsilon_{amp}\sigma R_0(\Delta T)^3/k_{amp}$$
$$V_p = V_g/U_0, \quad Ste = H/\Delta T C_p, \quad Ha = B_0 R_0\sqrt{\sigma_m/\rho_0 v}$$

The boundary conditions for the configuration considered are determined by the physical constraints and are detailed below:

$$T = 0 \quad \text{at } x = 0,\ L_1 \leqslant y \leqslant L_4 \tag{8}$$

$$T = 1 \quad \text{at } x = L_0,\ L_1 \leqslant y \leqslant L_4 \tag{9}$$

$$\hat{n} \cdot \nabla T = -Ra\lfloor (T + T_c^*)^4 - (T_{amb} + T_c^*)^4 \rfloor \quad \text{at } 0 \leqslant x \leqslant L_0,\ y = L_1 \text{ and } y = L_4 \tag{10}$$

$$\hat{n} \cdot \nabla T = (k_{amp}/k_{cry})(\hat{n} \cdot \nabla T_{amp}) \quad \text{at } 0 \leqslant x \leqslant h(y),\ y = L_2 \text{ and } y = L_3 \tag{11}$$

$$u = V_p, \quad v = 0, \quad \hat{n} \cdot \nabla C = 0 \tag{12}$$

$$\hat{n} \cdot \nabla T = (k_{amp}/k)(\hat{n} \cdot \nabla T_{amp}), \quad \text{at } h(y) \leqslant x \leqslant L_0,\ y = L_2 \text{ and } y = L_3 \tag{13}$$

$$u = V_p, \quad v = 0, \quad \hat{n} \cdot \nabla C = V_p Sc(C - 1)(\hat{n} \cdot \hat{e}_x) \quad \text{at } x = L_0,\ L_2 \leqslant y \leqslant L_3 \tag{14}$$

$$\hat{n} \cdot (\vec{U} - \vec{U}^*) = \hat{n} \cdot (\vec{U}_{cry} - \vec{U}^*)$$
$$\hat{n} \times (\vec{U} - \vec{U}_{cry}) = 0 \tag{15}$$

$$\hat{n} \cdot \nabla C = Sc[\hat{n} \cdot (\vec{U} - \vec{U}^*)C - \hat{n} \cdot (\vec{U}_{cry} - \vec{U}^*)C_{cry}] \tag{16}$$

$$T = T_m - mC, \tag{17}$$

$$(\hat{\boldsymbol{n}}\cdot\nabla T)-(k_{\mathrm{cry}}/k)(\hat{\boldsymbol{n}}\cdot\nabla T_{\mathrm{cry}})=Ste\,Pr\,\hat{\boldsymbol{n}}\cdot(\vec{U}_{\mathrm{cry}}-\vec{U}^{*})\quad \text{at } x=h(y),\ L_2\leqslant y\leqslant L_3 \tag{18}$$

where $T_{\mathrm{c}}^{*}=T_{\mathrm{c}}/\Delta T$, $C_{\mathrm{cry}}=k_0C$, $\hat{\boldsymbol{n}}\cdot\vec{U}_{\mathrm{cry}}=V_{\mathrm{p}}$, $\hat{\boldsymbol{n}}\,\vec{U}_{\mathrm{cry}}=0$.

3. The finite element solution

The governing equations described above along with the boundary conditions are solved using the deforming Galerkin finite element method. The stiffness matrix is obtained by using Galerkin's method of Weighted Residuals. The formulations and relevant benchmark tests were detailed in a series of papers published earlier [17,23] and thus only a brief summary is given here. The governing equations are recast in an integral form and the field variables are interpolated using shape functions over the computational domain. With an appropriate algebraic manipulation, the following set of equations are obtained:

$$\left(\int_\Omega \psi\,\widehat{i}\cdot\nabla\phi^{\mathrm{T}}\,\mathrm{d}V\right)\mathbf{U}_i=-\varepsilon\left(\int_\Omega\psi\psi^{\mathrm{T}}\,\mathrm{d}V\right)\mathbf{P} \tag{19}$$

$$\begin{aligned}&\left(\int_\Omega\phi\phi^{\mathrm{T}}\,\mathrm{d}V\right)\frac{\mathrm{d}\mathbf{U}_i}{\mathrm{d}t}+\left(\int_\Omega\phi\mathbf{u}\cdot\nabla\phi^{\mathrm{T}}\,\mathrm{d}V\right)\mathbf{U}_i\\&-\left(\int_\Omega\hat{\boldsymbol{i}}\cdot\nabla\phi\psi^{\mathrm{T}}\,\mathrm{d}V\right)\mathbf{P}+\left(\int_\Omega\nabla\phi\cdot\nabla\phi^{\mathrm{T}}\,\mathrm{d}V\right)\mathbf{U}_i\\&+\left(\int_\Omega(\hat{\boldsymbol{i}}\cdot\nabla\phi)(\hat{\boldsymbol{j}}\cdot\nabla\phi^{\mathrm{T}})\,\mathrm{d}V\right)\mathbf{U}_j\\&+\left(\int_\Omega\phi\theta^{\mathrm{T}}\mathbf{g}\,\mathrm{d}V\right)(\mathbf{T}-T_{\mathrm{m}})+\left(\int_\Omega\phi\theta^{\mathrm{T}}\mathbf{g}\,\mathrm{d}V\right)(\mathbf{C}-1)\\&=\int_{\partial\Omega}\mathbf{n}\cdot\tau\cdot\hat{\boldsymbol{i}}\phi\,\mathrm{d}S+\int_\Omega\phi Ha^2(\mathbf{u}\times\mathbf{B}\times\mathbf{B})\,\mathrm{d}V\end{aligned} \tag{20}$$

$$\left(\int_\Omega Pr\theta\theta^{\mathrm{T}}\,\mathrm{d}V\right)\frac{\mathrm{d}\mathbf{T}}{\mathrm{d}t}+\left(\int_\Omega Pr\theta\mathbf{u}\cdot\nabla\theta^{\mathrm{T}}\,\mathrm{d}V\right)\mathbf{T}+\left(\int_\Omega\nabla\theta\cdot\nabla\theta^{\mathrm{T}}\,\mathrm{d}V\right)\mathbf{T}=-\int_{\partial\Omega}q_{\mathrm{T}}\theta\,\mathrm{d}S \tag{21}$$

$$\left(\int_\Omega Sc\theta\theta^{\mathrm{T}}\,\mathrm{d}V\right)\frac{\mathrm{d}\mathbf{C}}{\mathrm{d}t}+\left(\int_\Omega Sc\theta\mathbf{u}\cdot\nabla\theta^{\mathrm{T}}\,\mathrm{d}V\right)\mathbf{C}+\left(\int_\Omega\nabla\theta\cdot\nabla\theta^{\mathrm{T}}\,\mathrm{d}V\right)\mathbf{C}=-\int_{\partial\Omega}q_{\mathrm{c}}\theta\,\mathrm{d}s \tag{22}$$

Once the form of shape functions ϕ, θ, and ψ for velocity, pressure and scalars are specified, the integrals defined in the above equations can be expressed in matrix form. Combining the momentum and energy equations into a single matrix equation gives rise to the following element stiffness matrix equation:

$$\begin{bmatrix}\mathbf{M}&0&0\\0&\mathbf{N}_{\mathrm{T}}&0\\0&0&\mathbf{N}_{\mathrm{C}}\end{bmatrix}\begin{bmatrix}\dot{\mathbf{U}}\\\dot{\mathbf{T}}\\\dot{\mathbf{C}}\end{bmatrix}+\begin{bmatrix}\mathbf{A}(\mathbf{U})+\mathbf{K}+\frac{1}{\varepsilon}\mathbf{E}\mathbf{M}_{\mathrm{p}}^{-1}\mathbf{E}^{\mathrm{T}}&\mathbf{B}_{\mathrm{T}}&\mathbf{B}_{\mathrm{C}}\\0&\mathbf{D}_{\mathrm{T}}(\mathbf{U})+\mathbf{L}_{\mathrm{T}}&0\\0&0&\mathbf{D}_{\mathrm{C}}(\mathbf{U})+\mathbf{L}_{\mathrm{C}}\end{bmatrix}\times\begin{bmatrix}\mathbf{U}\\\mathbf{T}\\\mathbf{C}\end{bmatrix}=\begin{bmatrix}\mathbf{F}\\\mathbf{G}_{\mathrm{T}}\\\mathbf{G}_{\mathrm{C}}\end{bmatrix} \tag{23}$$

Note that in constructing the above element matrix equation, the penalty formulation has been applied, and $\mathbf{P}$ in the momentum equation is substituted by $\frac{1}{\varepsilon}\mathbf{M}_{\mathrm{p}}^{-1}\mathbf{E}^{\mathrm{T}}\mathbf{U}$. The assembled global matrix equations are stored in the skyline form and solved using the Gaussian elimination method. The coefficient matrices of Eq. (23) above are calculated by

$$\mathbf{M}_{\mathrm{p}}=\int_\Omega\psi\psi^{\mathrm{T}}\,\mathrm{d}V;\quad \mathbf{N}_{\mathrm{T}}=\int_\Omega Pr\theta\theta^{\mathrm{T}}\,\mathrm{d}V$$

$$\mathbf{M}=\int_\Omega\theta\theta^{\mathrm{T}}\,\mathrm{d}\,\mathrm{d}V;\quad \mathbf{N}_{\mathrm{C}}=\int_\Omega Sc\theta\theta^{\mathrm{T}}\,\mathrm{d}V$$

$$\mathbf{E}_i=\int_\Omega\widehat{i}\cdot\nabla\phi\psi^{\mathrm{T}}\,\mathrm{d}V;\quad \mathbf{L}_{\mathrm{C}}=\int_\Omega\nabla\theta\cdot\nabla\theta^{\mathrm{T}}\,\mathrm{d}V$$

$$\mathbf{L}_{\mathrm{T}}=\int_\Omega\nabla\theta\cdot\nabla\theta^{\mathrm{T}}\,\mathrm{d}V;\quad \mathbf{A}(\mathbf{U})=\int_\Omega\phi\mathbf{u}\cdot\nabla\theta^{\mathrm{T}}\,\mathrm{d}V$$

$$\mathbf{D}_{\mathrm{C}}(\mathbf{U})=\int_\Omega Sc\theta\mathbf{u}\cdot\nabla\theta^{\mathrm{T}}\,\mathrm{d}V;\quad \mathbf{D}_{\mathrm{T}}(\mathbf{U})=\int_\Omega Pr\theta\mathbf{u}\cdot\nabla\theta^{\mathrm{T}}\,\mathrm{d}V$$

$$\mathbf{B}_{\mathrm{C}}=\int_\Omega Gr_{\mathrm{C}}(\mathbf{g}\phi\theta^{\mathrm{T}})\,\mathrm{d}V;\quad \mathbf{B}_{\mathrm{T}}=\int_\Omega Gr_{\mathrm{T}}(\mathbf{g}\phi\theta^{\mathrm{T}})\,\mathrm{d}V$$

$$\mathbf{G}_{\mathrm{C}}=-\int_{\partial\Omega}q_{\mathrm{C}}\theta\,\mathrm{d}S;\quad \mathbf{G}_{\mathrm{T}}=-\int_{\partial\Omega}q_{\mathrm{T}}\theta\,\mathrm{d}S$$

$$\mathbf{F}=\int_{\partial\Omega}\mathbf{n}\cdot\tau\phi\,\mathrm{d}S+\int_\Omega\phi Ha^2(\mathbf{u}\times\mathbf{B}\times\mathbf{B})\,\mathrm{d}V+\int_\Omega Gr_{\mathrm{C}}(\mathbf{g}\phi\theta^{\mathrm{T}})T_{\mathrm{m}}\,\mathrm{d}V+\int_\Omega Gr_{\mathrm{T}}(\mathbf{g}\phi\theta^{\mathrm{T}})\,\mathrm{d}V$$

$$\mathbf{K}_{ij}=\left(\int_\Omega\nabla\phi\cdot\nabla\phi^{\mathrm{T}}\,\mathrm{d}V\right)\delta_{ij}+\int_\Omega(\hat{\boldsymbol{i}}\cdot\nabla\phi)(\hat{\boldsymbol{j}}\cdot\nabla\phi^{\mathrm{T}})\,\mathrm{d}V$$

To implement the deforming finite elements to model the dynamic change of the moving interface, i.e., solidification front between the liquid and solid, a quasi-Lagrangian description is adopted. By this method, a region that covers the solidifying liquid and solid is defined and the nodes within the region are allowed to move in accordance with the interface movement. These additional velocities that result from the mesh movement are added to the velocity field as given in the above equations. The energy balance equation describing the latent heat release and interface change (Eq. (18)) is

directly integrated within the context of weighted residuals,

$$\left(\int_{\Omega}\theta\hat{\boldsymbol{n}}\cdot\nabla\theta^{\mathrm{T}}\,\mathrm{d}V\right)\mathbf{T}-\left(\int_{\Omega}(k_{\mathrm{cry}}/k)\theta\hat{\boldsymbol{n}}\cdot\nabla\theta^{\mathrm{T}}\,\mathrm{d}V\right)\mathbf{T}_{\mathrm{cry}}=-\int_{\partial\Omega}q_{\mathrm{T}}^{*}\theta\,\mathrm{d}S \tag{24}$$

which is applied as a surface energy source to the total thermal energy balance equation, and added to the right-hand side of Eq. (23). Two basic algorithms have been applied in the past. One treats the moving interface as a separate variable and the interface thermal boundary condition in this present case would then be incorporated into the global finite element matrix. The other treats the interface thermal boundary condition as a separate constraint and solved separately from the coupled field equations. Our numerical experience with these types of moving interface problems and solution algorithms shows that in a majority of cases the incorporation of the isothermal constraint into the global matrix results in a very unstable nonlinear system. The whole system is extremely sensitive to the boundary perturbations, more often than not, leading to divergence. Separation of the moving interface boundary coordinates from the global finite element solutions for field variables, however, requires the assurance of convergence of both moving interface coordinates and field variables in two related loops. For this case the global finite element matrix has a smaller bandwidth and thus requires a short CPU time for each iteration of field variable computations, which takes the majority of the computing time. Our tests further showed that the two methods require approximately the same CPU time, with the latter being much more robust and numerically stable. The latter has been used in the present study and for the results presented below. Also, there are two different methods used to track the liquid–solid interface and the results are the same within the machine accuracy. One method entails the use of the weighted residual method to integrate the interface thermal boundary condition (Eq. (17)), while the other use a directional search for the melting temperature after the coupled thermal, solute and fluid flow field calculations are converged. The latter is adopted in the present study.

In summary, our interface tracking strategy used in the present study involves an iterative procedure that entails applying the energy balance equation along the interface as a surface source and searching for the interface position coordinates based on each converged field calculations. The updated interface positions are the fed back to the field calculations until both the interface position coordinates and field variables are converged within a preset criterion, which is set at 1×10^{-4} for the results presented below.

4. Results and discussion

The finite element model described above permits the prediction of both steady and transient fluid flow, heat and mass transfer, along with the solidification interface shape in morphologically stable crystal growth systems under both terrestrial and microgravity conditions with and without the presence of magnetic field in the axial direction. The model development was based on the finite element code reported in early studies, for example [7,14,16–20], which include both code development and benchmark testing. While both the formulations and computer code are general and can be applied to both 2-D and 3-D calculations, our focus here is on a 2-D simplification of a cylindrical system for growing binary single crystals in a microgravity environment. The thermo-physical properties [6] and geometric dimensions for the study are given in Table 1. The studies used 2968 9-node elements with the increasing mesh distribution near the interface. The penalty pressure formulation was used to approximate the pressure field. Tests were conducted to ensure the numerical results are mesh independent to within a tolerance of 1% between two consecutively refined meshes. Numerical simulations were carried out for a wide range of conditions and a selection of the computed results is presented below.

4.1. Steady microgravity condition

Under an idealized microgravity condition, the gravity level is $10^{-6}g_0$. This condition may be obtained when the space vehicle follows the orbit perfectly without disturbances. Numerical simulations were carried out for this condition. The results are useful in helping to gain physical insight into the steady state behavior of the system. On the other hand, they provide the initial condition for the dynamic behavior of the system when g-jitter perturbations set in. The simulations were based on the direct numerical solution to the steady state governing equations by dropping out the time-dependent terms in the model equations described in Section 2 while keeping all the mutually coupled terms. For this case, the gravity is assumed to be oriented perpendicular to the growth direction, which represents the worst case. The computed results show that the flow field is nearly dominated by the pulling velocity with $U_{\max}=0.0576$, and the magnitude of the thermal and solutal gradient induced flow is small. The results are consistent with those obtained earlier from a simplified melt flow system where solidification was not considered [14], confirming that the simplified model indeed provides a good approximation to the melt flows under more realistic growth conditions, as they are intended to. The heat transfer in the melt pool is largely controlled by thermal conduction, which is a direct result of small Prandtl number for the system being studied. Solidification in-

Table 1
Parameters used for calculations [6]

Physics properties	
T_{m0}	544 K
ρ_0	10,070 kg m^{-3}
C_p	144.87 J kg^{-1} K^{-1}
ν	1.837×10^{-7} m^2 s^{-1}
D	2.7×10^{-9} m^2 s^{-1}
C_0	0.1 at.%
β_T	1.25×10^{-4} K^{-1}
β_C	−0.3049 (volume fraction)$^{-1}$
k_0	0.29 at.%/at.%
m	2.32 K/at.%
g_0	9.8 ms^{-2}
H	5.25×10^4 J kg^{-1}
k	12.4 W m^{-1} K^{-1}
k_{cry}	6.5 W m^{-1} K^{-1}
k_{amp}	2.01 W m^{-1} K^{-1}
κ	8.5×10^{-6} m^2 s^{-1}
κ_{cry}	4.5×10^{-6} m^2 s^{-1}
κ_{amp}	8.7×10^{-7} m^2 s^{-1}
ε_{amp}	0.8
System parameters	
W_i	6.0×10^{-3} m
W_o	1.0×10^{-2} m
L	4.2×10^{-2} m
L_h	4.95×10^{-3} m
L_c	4.95×10^{-3} m
L_g	3.21×10^{-2} m
dT/dx	2.0×10^4 K m^{-1}
T_h	973 K
T_c	323 K
V_g	-3.34×10^{-6} m s^{-1}
B_0	0.5T
Scale parameters	
U_0	6.12×10^{-5} m s^{-1}
ΔT	650 K
R_0	3×10^{-3} m
t_0	49.0 s
Non-dimensional parameters	
Pr	0.0215
Sc	68.0
Gr_T	6.37×10^5
Gr_S	-1.957×10^3
Ste	0.558
Ha	38.7
Ra	0.01859
T_m	0.34
V_p	−0.055
T_c^*	0.497

terface position and temperature and solute concentration distributions along the solidification interface for the steady case are shown in Fig. 2. It can be seen that the interface is concave into the solid phase because the crystal loses heat through the two sides (Fig. 2a), and the melting temperature is no longer constant along the interface (Fig. 2b). With the flow field described above and the concave interface, the solute concentration along the interface would be non-uniform with a maximum around the center of the interface. The solute concentration non-uniformity at the interface is about 7% measured by $(C_{max} - C_{min})/C_{average}$ along the growth interface (Fig. 2c). The effects of the solute concentration dependent melting temperature on the system performance are also shown in Fig. 2. It can be seen that with the concentration effects considered, the melting temperature is no longer a constant, which results in a noticeable change in the solidification interface position and the solute concentration non-uniformity at the interface. The above results clearly illustrate that it is crucial to include the concentration dependent melting temperature to accurately predict the solidification phenomena in the present system.

4.2. Single frequency g-jitter

Single frequency g-jitter represents an idealized perturbation to a mcirogravity environment. The Fourier analysis of g-jitter data collected by on-board accelerometers indicates that g-jitter has a wide range of frequency spectrum. However, space flight experiments with single crystal growth suggest that only the low frequency g-jitter produces deleterious effects on the quality of the crystals. A single component g-jitter force provides a valuable means for developing a fundamental understanding of physics governing the effects of gravity perturbation on convection and solidification phenomena associated with space melt growth of crystals. The single frequency g-jitter perturbation, $g(t) = 10^{-3}g_0\sin(0.2\pi t)$ oriented perpendicular to the thermal gradient is used in the present study. The computed results show that the flow field oscillates with time and reaches the quasi-steady state eventually. The fluid field variations in a time harmonic cycle are shown in Fig. 3. It can be seen that a strong convection loop develops in the melt pool, which covers the entire pool region. The convection loop oscillates and reverses its rotating direction with time at approximately the same frequency as the driving g-jitter perturbations. The strong flow sweeps along the solid–liquid interface, and its effect on the concentration distribution in the melt is shown in Fig. 4, where an appreciable concentration striation is detected. The corresponding interface shapes and temperature and solute concentration distributions along the interface are plotted in Fig. 5, where the initial condition (steady microgravity condition) is plotted as a comparison. It can be seen that the g-jitter induced convection sweeps along the solidification interface and screws the temperature minimum and the solute concentration maximum at the interface more close to $y = 2$ compared with the steady case. However, when the quasi-steady state is reached, the interface shape and temperature and solute

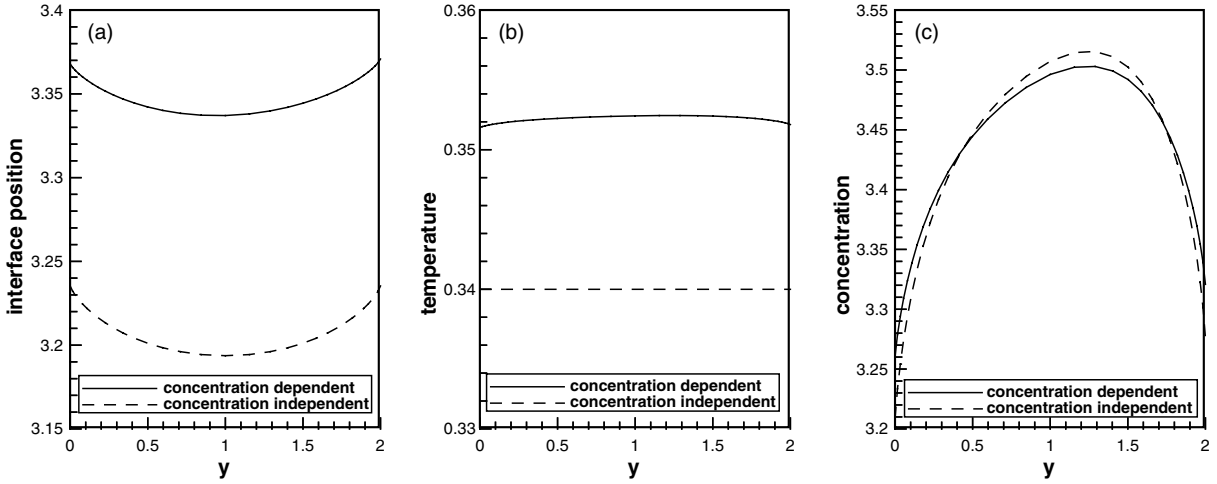

Fig. 2. (a) Interface positions, (b) temperature distributions and (c) solute concentration distributions along the solidification interface for steady cases with and without concentration effect. All variables are dimensionless.

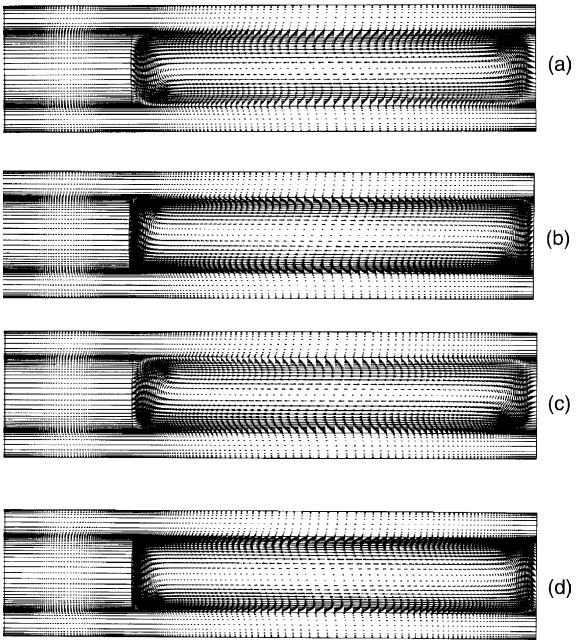

Fig. 3. Flow field development caused by a single frequency g-jitter in a time harmonic cycle in absence of magnetic field: (a) $t = 3.876$, $U_{max} = 0.6161$; (b) $t = 3.927$, $U_{max} = 0.6922$; (c) $t = 3.978$, $U_{max} = 0.6161$; (d) $t = 4.029$, $U_{max} = 0.6920$.

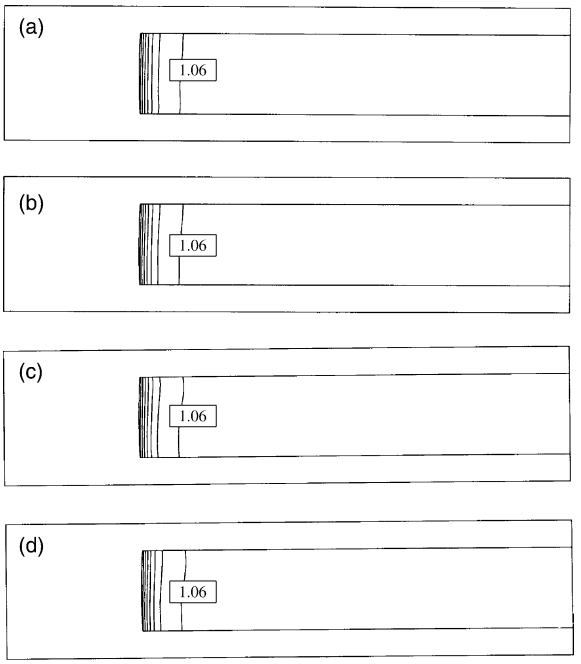

Fig. 4. Concentration distribution development caused by a single frequency g-jitter in a time harmonic cycle in absence of magnetic field: (a) $t = 3.876$; (b) $t = 3.927$; (c) $t = 3.978$; (d) $t = 4.029$. From left to right, $C_{max} = 3.52$ reduced to $C = 1.06$, $\Delta C = 0.35$.

concentration distributions along the interface are nearly unchanged with time. For practical applications, the velocity components (u, v) of the melt flow and the solute concentration in the region near the solidification interface are crucial because of their direct implication to crystal quality. The evolutions of these field variables at the point in the melt near the growth front are shown in Fig. 6. It is seen from the results that the velocity components oscillate with time at the nearly same frequency of the driving g-jitter force when the quasi-steady state is reached, and so does the solute concentration oscillation.

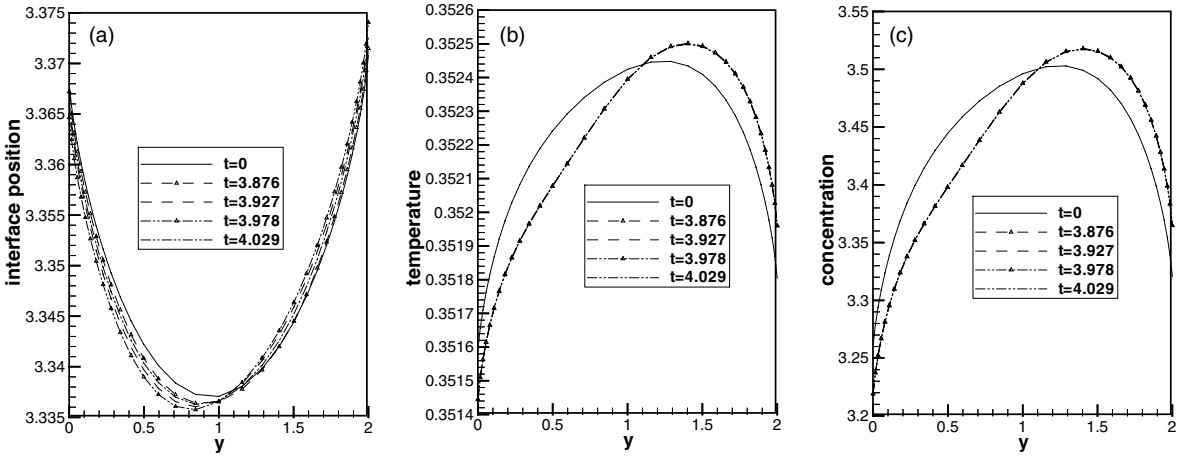

Fig. 5. The development of (a) the interface positions, (b) the temperature and (c) concentration distributions along the growth interface caused by a single frequency g-jitter in a time harmonic cycle in absence of magnetic field. All variables are dimensionless.

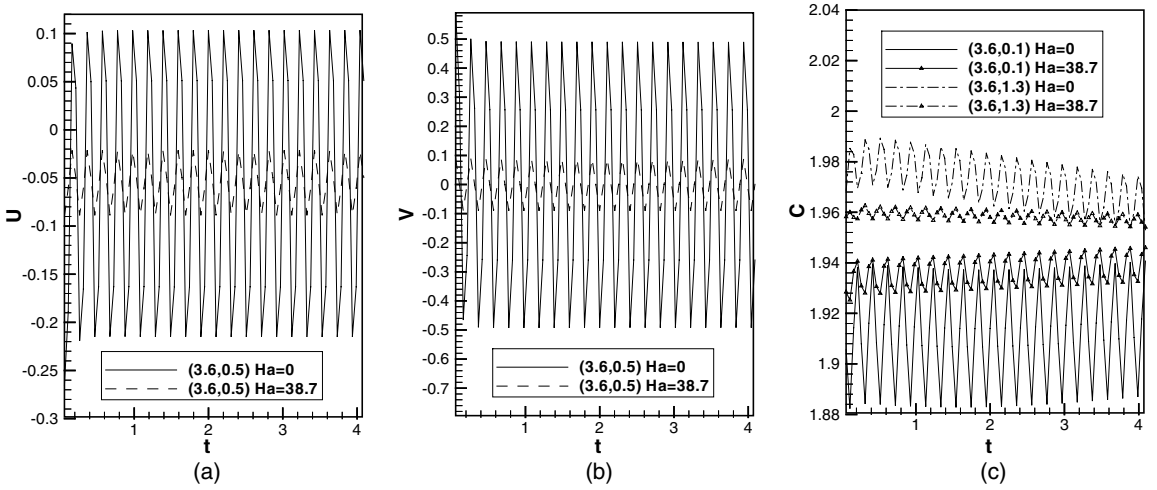

Fig. 6. Time evolution of velocity components and solute concentration at selected points in the melt near solidification interface caused by a single frequency g-jitter with and without magnetic field: (a) $x = 3.6$, $y = 0.5$; (b) $x = 3.6$, $y = 0.5$; (c) $x = 3.6$, $y = 0.1$ and $x = 3.6$, $y = 1.3$.

One of the important findings obtained from a previous study on the melt flow is that a DC magnetic field is useful in suppressing the deleterious convection effects induced by g-jitter in a microgravity environment. Numerical simulations, using the finite element model, were conducted for the same single frequency g-jitter perturbation but with an imposed magnetic field. In sharp contrast to the case without an applied field, the convection is substantially reduced by the applied magnetic field, and the convection cell is limited in the central region of the melt pool (see Fig. 7). This change of the flow field has greatly improved the concentration uniformity in the melt near the solidification front, as appear in Fig. 8. The corresponding interface shape, temperature and concentration distributions along the interface in a time harmonic cycle in presence of the applied magnetic field are given in Fig. 9. Here it is clear that all the deviations from the steady state resulting from the g-jitter induced convection are almost entirely eliminated. The effectiveness of the applied magnetic field in suppressing the g-jitter induced convective flows is further illustrated in Fig. 6, where the evolution of the velocity components and solute concentration at the same point in the melt near the solidification front in presence of the applied magnetic field are also plotted. It is seen that the applied magnetic field results in a significant reduction of the flow velocity components and the solute concentration variation. However, the applied

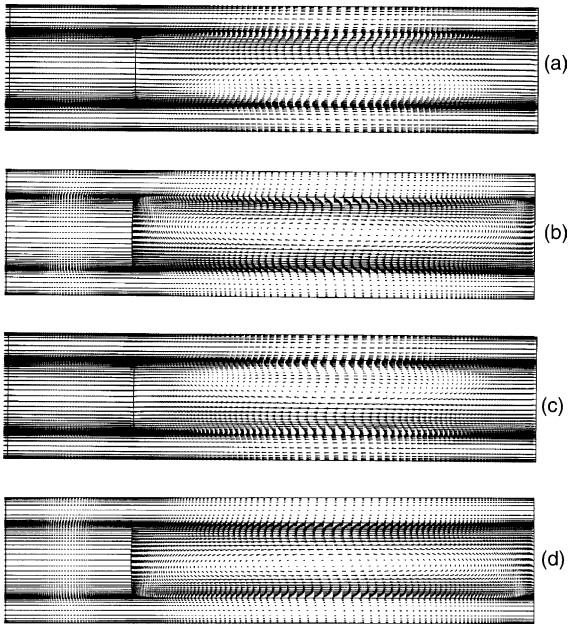

Fig. 7. Flow field development caused by a single frequency g-jitter in a time harmonic cycle in presence of magnetic field: (a) $t = 3.876$, $U_{max} = 0.1603$; (b) $t = 3.927$, $U_{max} = 0.5483$; (c) $t = 3.978$, $U_{max} = 0.1603$; (d) $t = 4.029$, $U_{max} = 0.5483$.

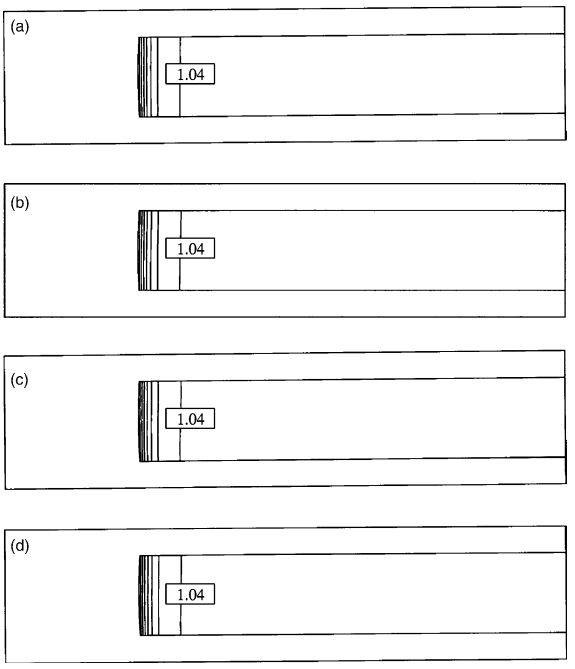

Fig. 8. Concentration distribution development caused by a single frequency g-jitter in a time harmonic cycle in presence of magnetic field: (a) $t = 3.876$; (b) $t = 3.927$; (c) $t = 3.978$; (d) $t = 4.029$. From left to right, $C_{max} = 3.50$ reduced to $C = 1.04$, $\Delta C = 0.35$. All variables are dimensionless.

magnetic field would not change the frequency of the time oscillation but only the amplitude of the oscillation. This is consistent with the conclusions obtained from the study of melt flow without solidification [14].

4.3. Real g-jitter

As stated earlier, real g-jitter perturbations are primarily random in direction, orientation and magnitude. Control of convection generated by these random gravity signatures is of critical importance to high quality single crystal growth. With the model as described above, the use of the magnetic fields in controlling the convective flows and hence the solidification behavior can be assessed for more realistic space flight conditions. The numerical simulations were conducted using the g-jitter data taken by an on-board accelerometer during a space flight (Fig. 10). As expected, these random gravity forces will cause convective flows in the melt pool and convection cells developed also vary with time. However, the flows generated by these gravity signatures will not produce a regular, time harmonic oscillation cell as shown above for single frequency g-jitter forces. Analyses of the computed results show that an applied magnetic field has strong effects on the suppression of these convective flows that vary randomly with time. Fig. 11 shows the time variation of field variables (u, v and c) at the point in the melt near the solidification interface. Here, the g-jitter induced convection cell varies irregularly with time to reflect the nature of the g-jitter driving forces. The spikes of velocities emerge in response to the g-jitter perturbations during the space flight, which in turn cause irregular changes in solute distribution. The irregularities in velocity and concentration cause an increase in the nonuniformity of solute concentration distribution along the solidification interface (Fig. 12) and are responsible for inconsistent qualities of crystals grown in space.

In presence of the applied magnetic field, the velocity spikes are substantially damped and the concentration variation is henceforth reduced (Fig. 11). An examination of the results also shows that the applied magnetic field is more effective in damping the large amplitude velocity spikes, which confirms the conclusions reached by analytical and numerical solutions performed for simplified melt flow systems [14]. The dynamic evolution of the solid–liquid interface and concentration striation along the interface as a result of g-jitter induced convection with and without an imposed magnetic field is compared in Fig. 13. The results are selected for a few moments at which the velocities experience spikes (see Fig. 11). As a further comparison, the initial interface shape is also plotted. It transpires that g-jitter can have a noticeable, though small, effect on the interface position but may strongly perturb the concentration field near the interface. The effects of the applied magnetic field on

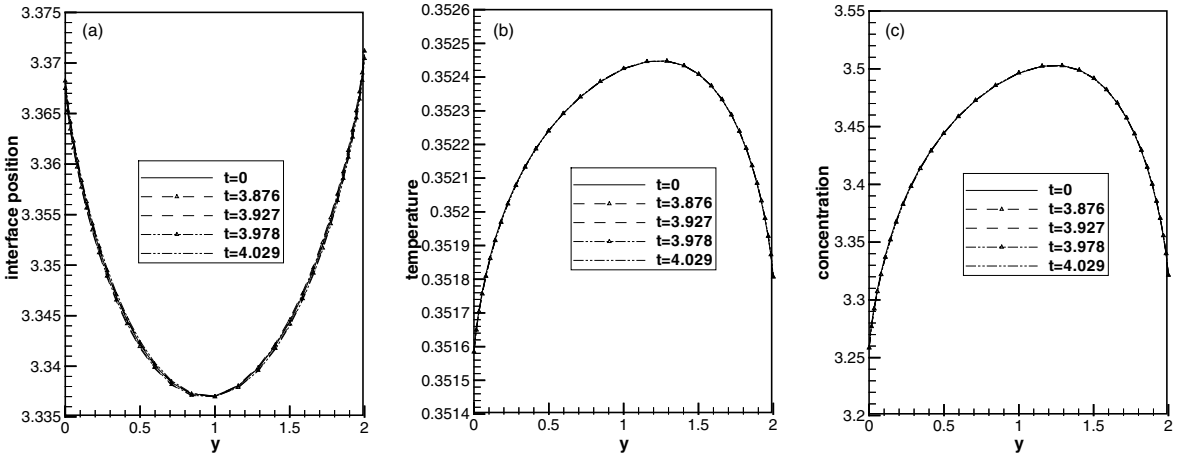

Fig. 9. The development of (a) interface positions, (b) the temperature and (c) concentration distributions along the growth interface caused by a single frequency g-jitter in a time harmonic cycle in presence of magnetic field.

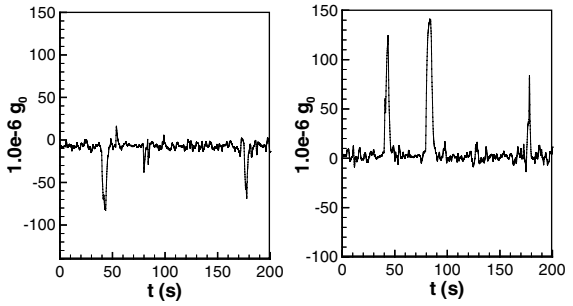

Fig. 10. Real g-jitter signatures in (a) x-direction and (b) y-direction taken by an on-board accelerometer during a space flight.

the time variation of the solute concentration non-uniformity along the solidification interface are shown in Fig. 12. Notice that the aggravations induced by g-jitter forces are nearly smoothed out by applying an appropriate magnetic field.

5. Concluding remarks

This paper presented a 2-D finite element model for the melt growth of single crystals in a microgravity environment with a superimposed magnetic field. The model is based on the deforming finite element methodology and is capable of predicting the phenomena of

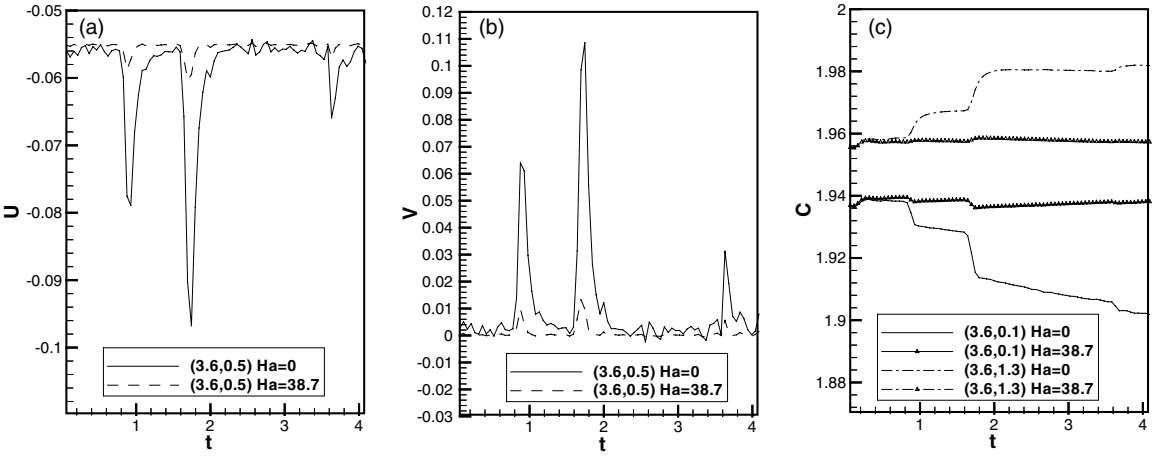

Fig. 11. Time evolution of velocity components and solute concentration at selected points in the melt near solidification interface caused by real g-jitter with and without magnetic field: (a) $x = 3.6$, $y = 0.5$; (b) $x = 3.6$, $y = 0.5$; (c) $x = 3.6$, $y = 0.1$ and $x = 3.6$, $y = 1.3$. All variables are dimensionless.

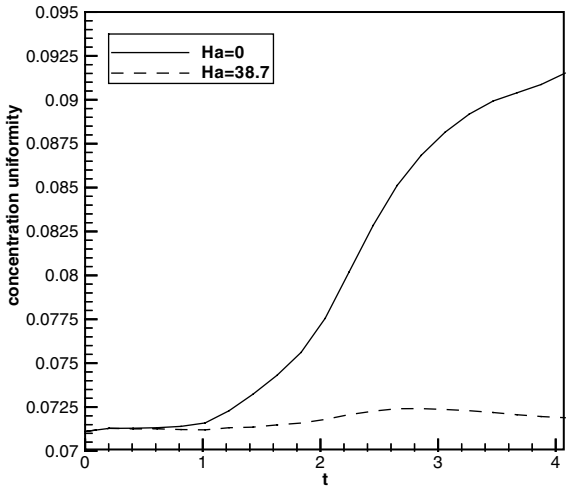

Fig. 12. The evolution of the concentration non-uniformities along the growth interface with and without the applied magnetic field, which measured by $(C(t)_{\max} - C(t)_{\min})/C(t)_{\text{average}}$.

steady state and transient melt convective flows, heat transfer and solute distribution, and solidification interface morphology associated with single crystal growth in microgravity with and without an applied magnetic field. The field variables are solved in a completely coupled fashion, with allowance made for the effects of solute on the melting temperature. Numerical simulations were carried out for a wide range of parameters including the idealized microgravity condition, synthesized g-jitter and also real g-jitter data taken by onboard accelerometers during a space flight. The results show that the time varying g-jitter disturbances, although small in magnitude, indeed cause an appreciable convective flow in the melt pool, which in turn produces detrimental effects during space growth of single crystals. An applied magnetic field of appropriate strength, superimposed on the microgravity, can provide a viable means to suppress or eliminate (i.e. suppress beyond detection) the deleterious effects resulting from the g-jitter disturbance. It is important to notice that the conclusion is made from the significant simplified mode

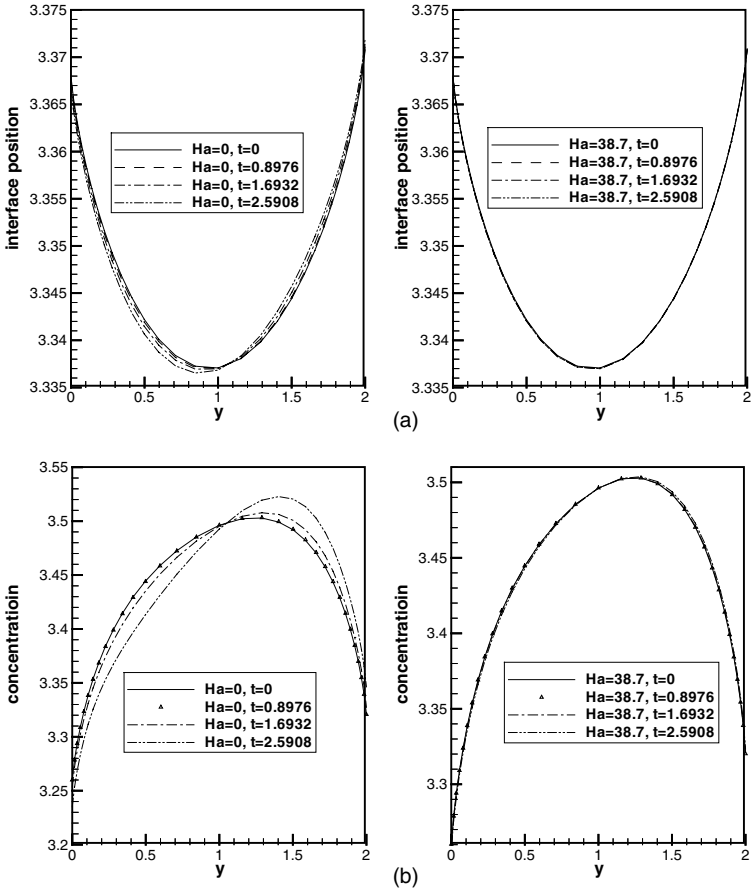

Fig. 13. The development of (a) growth interface positions and (b) the concentration distributions along the growth interface caused by real g-jitter without and with magnetic field at the selected time.

to the 3-D situation, so its validity when extended to the real 3-D situation is under research.

Acknowledgements

The authors are grateful for the financial support of this work by the NASA Microgravity Science and Application Division (Grant No. NAG8-1693).

References

[1] B.N. Antar, V.S. Nuotio-Antar, Fundamentals of Low Gravity Fluid Dynamics and Heat Transfer, CRC Press, Boca Ration, FL, 1993.
[2] H.C. de Groh III, E.S. Nelson, On residual acceleration during space experiments, ASME Winter Annual Meeting, Chicago, November 6–11, HTD-vol. 290, 1994, pp. 23–33.
[3] S. Schneider, J. Straub, Influence of the Prandtl number on laminar natural convection in a cylinder caused by *g*-jitter, J. Crystal Growth 97 (1989) 235–242.
[4] J.I.D. Alexander, S. Amiroudine, J. Quazzani, F. Rosenberger, Analysis of the low gravity tolerance of the Bridgman–Stockbarger crystal growth II: transient and periodic accelerations, J. Crystal Growth 113 (1991) 21–38.
[5] J.I.D. Alexander, J. Quazzani, F. Rosenberger, Analysis of the low gravity tolerance of the Bridgman–Stockbarger crystal growth I: steady and impulse accelerations, J. Crystal Growth 97 (1989) 285–302.
[6] M.W. Yao, R. Raman, H.C. de Groh, Numerical Simulation of Heat and Mass Transport During Space Crystal Growth With MEPHISTO, NASA TM 107015, 1995.
[7] B.Q. Li, Stability of modulated-gravity-induced thermal convection in magnetic fields, Phys. Rev. E 63 (2001) 416–514.
[8] W. Zhang, J. Casademunt, J. Venals, Study of parametric oscillator driven by narrow-band noise to model the response of a fluid surface to time-dependent acceleration, J. Phys. Fluids A 5 (1993) 3147–3152.
[9] A.A. Wheeler, G.B. Mcfadden, B.T. Murray, S.R. Coriell, Convection stability in Rayleigh-benard and directional solidification problems: high frequency gravity modulation, J. Phys. Fluids A 3 (1991) 2847–2853.
[10] J.I.D. Alexander, Low-gravity experiment sensitivity to residual acceleration: a review, Microgravity Sci. Tech. 2 (1994) 131–135.
[11] J. Baumgartl, M. Gewald, R. Rupp, J. Stierlen, G. Muller, in: Proc. of VIth Euro. Symp. on Materials and Fluids Sciences in Microgravity, Oxford, UK, pp. 47–52, 1990.
[12] N. Ma, J.S. Walker, Magnetic damping of buoyant convection during semiconductor crystal growth in microgravity: spikes on residual acceleration, Phys. Fluids 8 (4) (1996) 944–949.
[13] C. Benjapiyaporn, V. Timchenko, E. Leonardi, G. De Vahl Davis, H.C. de Groh III, Effects of space environment on flow and concentration during directional solidification, NASA TM 209293, 2000.
[14] B. Pan, D.Y. Shang, B.Q. Li, H.C. de Groh III, Magnetic damping effects on *g*-jitter driven melt convection and mass transfer in microgravity, Int. J. Heat Mass Transfer 45 (2002) 125–144.
[15] J. Baumgartl, G. Muller, The use of magnetic fields for damping the action of gravity fluctuations (*g*-jitter) during crystal growth under microgravity, J. Crystal Growth 169 (1996) 582–586.
[16] D.Y. Shang, B.Q. Li, H.C. de Groh III, Magnetic damping of *g*-jitter driven flows: 3-D calculations, J. Jpn. Soc. Microgravity Appl. 15 (Suppl. II) (1998) 108–113.
[17] B. Pan, B.Q. Li, Effects of magnetic field on oscillating mixed convection, Int. J. Heat Mass Transfer 41 (1998) 2705–2710.
[18] B.Q. Li, Stability of modulated-gravity-induced thermal convection in a magnetic field, Phys. Rev. E 63 (2001) 041508-1–041508-9.
[19] Y. Shu, B.Q. Li, H.C. de Groh, Magnetic damping of *g*-jitter induced double diffusive convection in microgravity, Numer. Heat Transfer A 42 (2002) 345–364.
[20] B.Q. Li, R. He, Computational modeling of electrodynamic and transport phenomena under terrestrial and microgravity conditions, Int. J. Appl. Electromagn. Mech. 14 (2002) 459–466.
[21] J. Honda, C. Zhang, B.Q. Li, H.C. de Groh, A 3-d model for magntic damping of *g*-jitter induced convection and solutal transport in a simplified Bridgmann configuration, in: Proceedings of the ASME Heat Transfer Division, New York, NY, November 2001.
[22] D.H. Kim, P.M. Adornato, R. Brown, Effect of vertical magnetic field on convection and segregation in vertical Bridgman crystal growth, J. Crystal Growth 89 (1988) 339–356.
[23] S.P. Song, B.Q. Li, Surface deformation and Marangoni flow in electrostatically levitated droplets, Int. J. Heat Mass Transfer 43 (2000) 3589–3606.